

**Sliding Friction of a Pillar Array Interface: Part I**

Journal:	<i>Soft Matter</i>
Manuscript ID	SM-ART-10-2023-001323.R1
Article Type:	Paper
Date Submitted by the Author:	16-Dec-2023
Complete List of Authors:	Kaur, Jasreen; Lehigh University, Chemical & Biomolecular Engineering Xiao, Xuemei; Cornell University, Department of Mechanical and Aerospace Engineering Khripin, Constantine; Michelin North America Inc Hui, Chung-Yuen; Cornell University, Theoretical and Applied Mechanics Jagota, Anand; Lehigh University, Bioengineering; Lehigh University, Department of Chemical & Biomolecular Engineering

Sliding Friction of a Pillar Array Interface: Part I

Jasreen Kaur¹, Xuemei Xiao², Constantine Khripin³, Chung-Yuen Hui^{2*}, Anand Jagota^{1,4*}

¹ Department of Chemical & Biomolecular Engineering, Lehigh University, Bethlehem, PA 18015, USA.

² Department of Mechanical and Aerospace Engineering, Cornell University, Ithaca, NY 14853, USA. E-mail: * ch45@cornell.edu

³ Michelin Americas Research Center, Michelin North America Inc., Greenville, SC, 29605, USA

⁴ Department of Bioengineering, Lehigh University, Bethlehem, PA 18015, USA, E-mail: * anj6@lehigh.edu

Keywords: Shape-complementary, bio-inspired, dislocations, friction, pillar

Abstract

Biology is replete with examples, at length scales ranging from the molecular (ligand-receptor binding) to the mesoscopic scale (wing arresting structures on dragonflies) where shape-complementary surfaces are used to control interfacial mechanical properties such as adhesion, friction, and contact compliance. Related bio-inspired and biomimetic structures have been used to achieve unique interfacial properties such as friction and adhesion enhancement, directional and switchable properties. The ability to tune friction by altering surface structures offers advantages in various fields, such as soft robotics and tire manufacturing. Here, we present a study of friction between polydimethylsiloxane (PDMS) samples with surfaces patterned with pillar-arrays. When brought in contact with each other the two samples spontaneously produce a Moiré pattern that can also be represented as an array of interfacial dislocations that depends on interfacial misorientation and lattice spacing. Misorientation alone produces an array of screw dislocations, while lattice mismatch alone produces an array of edge dislocations. Relative sliding motion is accompanied by interfacial glide of these patterns. The frictional force resisting dislocation glide arises from periodic single pillar-pillar contact and sliding. We study the behavior of pillar-pillar contact with larger (millimeter scale) pillar samples. Inter-pillar interaction measurements are combined with a geometric model for relative sliding to calculate frictional stress that is in good agreement with experiments.

1. Introduction

Achieving tunable adhesion and friction has applications ranging from rubber processing in tire manufacturing to object handling in soft robotics [1, 2]. Nature has provided us with many examples[3-6] of how microstructures on the surface can help control adhesion and friction. One such example is that of gecko [4, 7, 8], which has fibrillar structures on its toes to help it climb rough and smooth surfaces [5, 9, 10]. Geckos stick using Van der Waals dispersion forces [11] and have reversible adhesion [12]. Another such example is that of the head arresting system in dragonflies [13], which consists of intricate complementary microstructures on their head and neck to immobilize the head during tandem flight. Pillars in insects and amphibians have liquid secretion [14, 15] to form a capillary bridge for adhesion. Many other animals like skinks [16] and insects like beetles, spiders [17-19] have microstructures on their contacting surfaces to achieve desired adhesion and friction.

Bioinspired and biomimetic structures have been shown to modulate adhesion[20-22], friction[23], and contact compliance [6, 24-28] and to provide new functionality such as switchability and directional properties just by altering surface structures. An exemplary instance is the renowned case of Velcro [29], which operates on a loop-clasp mechanism. There is now a considerable literature on bioinspired contact surfaces [3, 9, 14, 15, 20, 30-38].

Most bioinspired studies focus on adhesion/ friction enhancement for microstructures on one side against a generic smooth or rough surface on the other [38, 39]. Shape complementary microstructures on both sides [40-44] of the interface have been relatively less explored. It has been demonstrated that shape complementarity at the micron scale can significantly enhance adhesion selectivity [40, 43, 45]. Guduru [46, 47] explored the mechanics of detachment between a wavy elastic surface and a rigid solid, uncovering an intriguing phenomenon. Surface waviness induces an unstable detachment process with alternating stable and unstable segments, resulting in increased work of separation. These findings provide an alternative explanation for the sometimes observed increase in pull-off force on rough surfaces. Adhesion selectivity using rippled surfaces [45] showed how shape complementary surfaces can enhance adhesion. Singh et al. used microchannel structures [43] to show adhesion enhancement in such shape complementary interfaces. Chen et al. [40] showed the same using a pillar geometry.

The investigation of sliding friction in shape-complementary surfaces has been relatively limited. Amonton's and Coulomb's laws describe friction in phenomenological terms, but the understanding of the relationship between macroscopic frictional response and the behavior of microscopic contacts remains under active investigation [48-50]. He et al. [42] studied sliding friction in ridge-channel and pillar interfaces, achieving friction enhancement in structured surfaces as compared to control surfaces. They reported the spontaneous formation of interfacial dislocations and presented a model for friction in ridge-channel surfaces based on treating the dislocation core as a crack. However, they presented only a qualitative description of friction in pillar surfaces.

For periodically structured two-sided interfaces, orientational or lattice-parameter mismatch leads to spontaneous production of Moiré patterns on the interface, much like an incommensurate twist grain boundary in crystalline solids. These can also be represented as dislocation structures in shape complementary surfaces that resemble microscale replicas of dislocations on the atomic scale in crystalline solids. Therefore, models for dislocation glide and microscopic friction mechanisms are relevant. For instance, the Peierls/Nabarro model for the dislocation core provides expressions for the minimum stress needed for dislocation glide [51, 52]. The Prandtl-Tomlinson model [53] for nanoscale friction is a minimalistic model for the relationship between the energy of interaction between two surfaces and friction [50, 54]. Related ideas have been used to explain friction in soft materials [55-57]. The Frenkel-Kontorova (FK) model is similarly based on motion of a chain of particles placed on a periodic substrate and is used to describe sliding in crystalline interfaces. This model can be used to understand a pillar interface, where each pillar has to slide past pillars on the other side of the interface [50, 58].

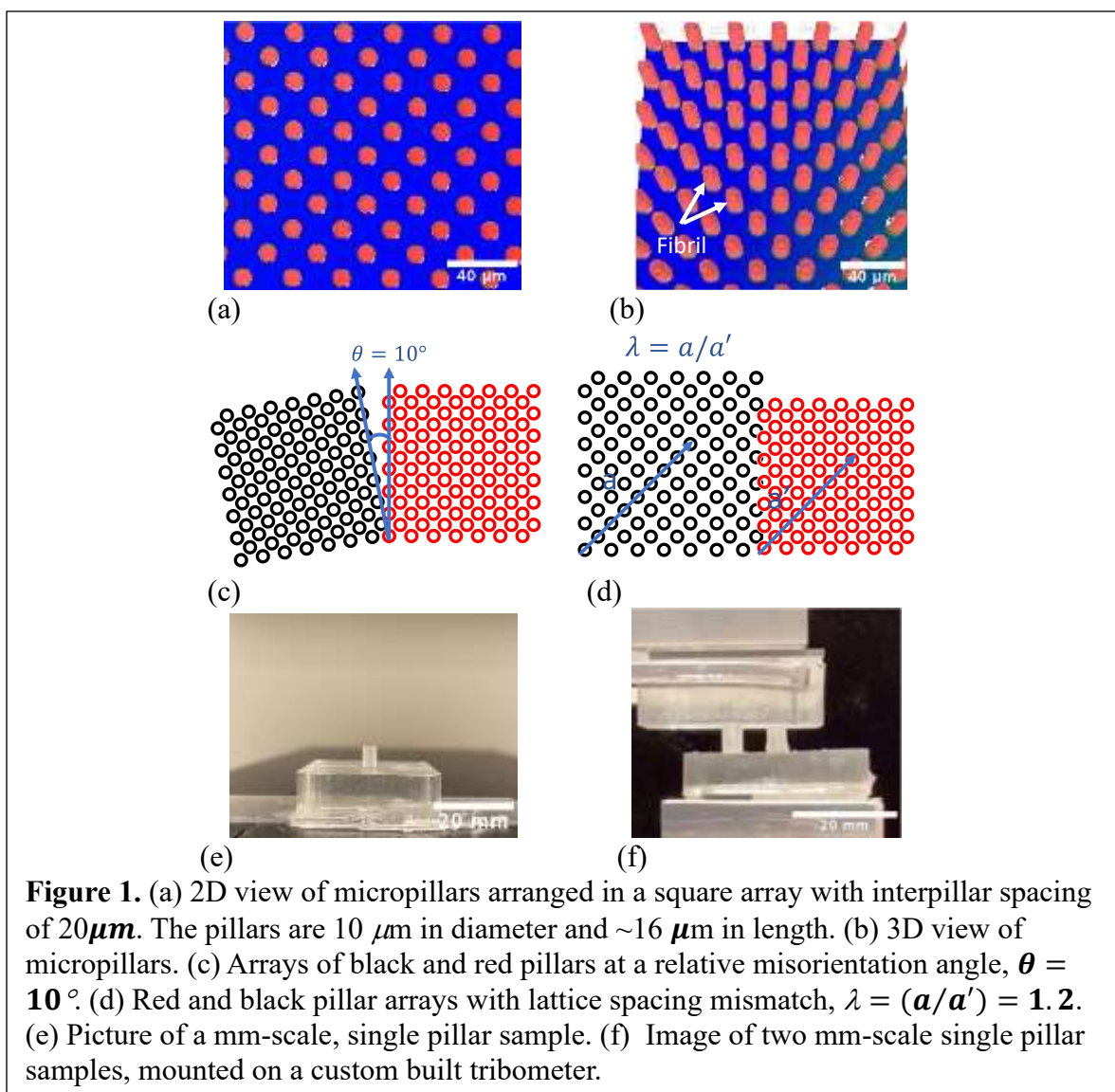
In this work we study friction in bioinspired, two-sided, micropillar surfaces. Our goal is to relate macroscopically measured friction stress, in terms of the pillar deformation at the interface. This problem is analogous to that of determining the stress needed for a dislocation to glide in a crystal, the basic version of which is determined by the Peierls-Nabarro model of the dislocation [51, 52, 54, 58-60]. Analogously, for our model, friction is defined as the force required for , Moiré patterns/dislocations to slide across the interface, the details of which depend on pillar-pillar interaction.

2. Experimental Methods

2.1 Sample Fabrication

Micropillar samples were fabricated using polydimethylsiloxane (PDMS) elastomer molded into an etched silicon master with pillar geometry on the surface patterned by photolithography. The pillars fabricated were 10 μm in diameter, 16 μm in height, and arranged in a square array with a minimum interpillar spacing of 20 μm . PDMS precursor (silicone elastomer base) was combined with crosslinker (curing agent, Sylgard 184 Silicone Elastomer kit, Dow Corning) in the ratio 10:1 by weight. The mixture was then degassed under vacuum for 30 minutes before applying to the master and was cured at room temperature for 2 days. The cured PDMS was then peeled off the silicon master. A typical sample is 30 mm long, 10 mm wide and about 800 μm thick. The second complementary sample was fabricated in a similar way. Additional samples were fabricated in a similar way but cured at different temperatures to introduce slightly different interpillar spacing due to differences in thermal contraction from curing to room temperature. Flat samples were also fabricated with no micropatterns and used for control experiments. A white light interferometry-based optical profilometer (Zegage, Zygo Corp) was used to produce micrographs of micropillar samples as shown in Fig. (1a, 1b). Figures 1c, 1d show a plan view of the interface each patterned with micropillars showing a misorientation, θ (Fig 1c) or a lattice mismatch, λ (Fig. 1d) between the two arrays. The circles represent the bottom of the pillars where they join the bulk. Figure 1c shows two pillar arrays (black and red lattices), in which the black lattice is rotated by a misorientation angle, $\theta=10^\circ$, with respect to the red lattice. Figure 1d shows two lattices with

different minimum spacings a and a' where $\lambda = a/a'$ is the lattice mismatch. (In the case shown here, $\lambda = 1.2$.)

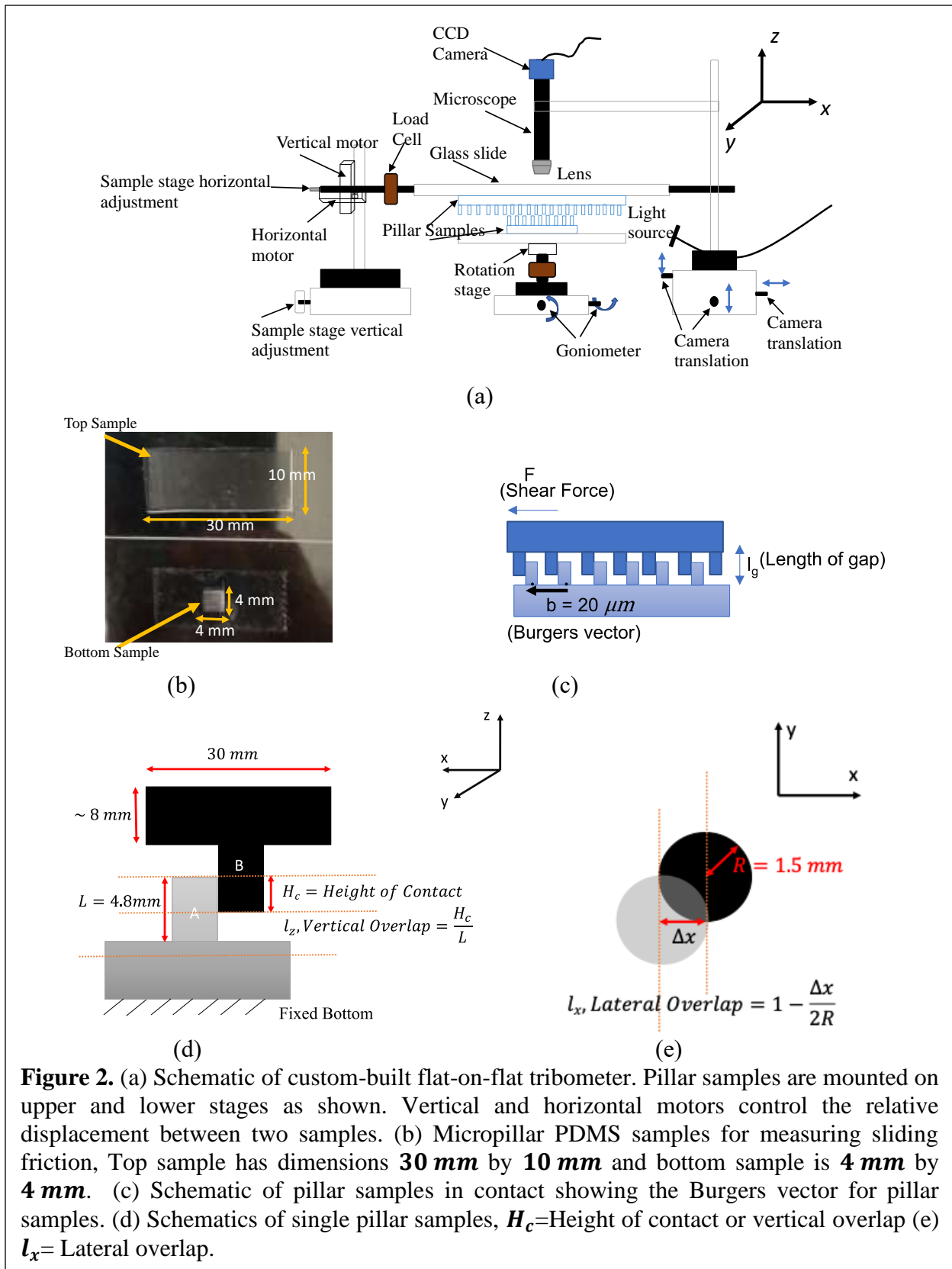


In order to study inter-pillar interaction, larger, mm-scale, single pillar samples were fabricated, as shown in Fig. 1(e), with the same aspect ratio as the micropillars. The process included using the same PDMS mixture and pouring the mixture into a mold fabricated for this purpose. The cured single pillar samples were 3 mm in diameter and 4.8 mm in height with backing dimensions of $30\text{ mm} * 30\text{ mm} * 8\text{ mm}$ shown in Fig. 1e and 1f. Details of the single pillar experiments and its analysis are given in the companion paper.

2.2 Friction Measurement

Friction measurements were conducted using a custom built Flat-on-Flat Tribometer as shown in Figure 2a. The setup consists of two stages on which samples are mounted, and a load cell each to measure horizontal or shear force, and vertical or normal force. Vertical and horizontal motors control the respective movement of stages, and the rotation motor controls rotation of the lower stage (to control misorientation). The motors are connected to a motion controller and the entire system is controlled by custom-written LabVIEW code. A camera is used to image the behavior of pillars at the interface during sliding.

Sliding friction was measured at five different values of misorientation ($\theta = 0^\circ, 5^\circ, 15^\circ, 30^\circ, 45^\circ$) and five different normal loads (0.075 N to 0.4 N) for patterned and flat control samples and each experiment was repeated three times. The setup can work under normal load or displacement control. Normal load is controlled by normal displacement, which is fed to the PID controller operated by LabVIEW software. The two samples are brought in contact using the vertical motor.



A typical friction experiment consists of sticking the top and bottom samples to glass slides using

double-sided Scotch® tape. The slides are mounted onto the lower and upper stages and brought into contact under displacement control (Fig 2a). After mounting the samples on the stage, we set the misorientation angle between the two samples using the rotation motor. We start by aligning the two samples at 0° misorientation, which is when dislocations disappear from the interface. With this as $\theta = 0^\circ$, other angles are easily obtained. Once we have the desired misorientation, we set a normal load and switch to normal load control. When the load stabilizes to the set value, we slide the samples with respect to each other for 3 mm at a velocity of 0.01mm/s.

3. Results and Discussion

3.1 Moiré Patterns & Dislocations

When the two micropillar samples are first brought in contact, Moiré patterns appear spontaneously on the interface, as we've reported previously[41-43]. Due to the square patterning and periodicity, the interface consists of periodic square regions, and the size of these regions depends on the misorientation and lattice spacing mismatch.[42, 61] The boundary of each square region can be viewed as a dislocation line, albeit with a diffuse core. Specifically, these regions are formed by two parallel sets of mutually perpendicular dislocation lines (see Figure 3). We refer to the edges in the Moiré patterns as "dislocation lines" by analogy to twist grain boundaries in crystals[61, 62]. Although they are geometrically similar to twist grain boundaries, the mechanics of interaction across the interface is different as discussed later.

The Moiré pattern and its accompanying dislocation array forms during the initial application of normal load, with density and orientation depending on λ and θ values. Orientational mismatch alone, ($\theta > 0^\circ$ at $\lambda=1$), produces an array of screw dislocations whereas a lattice mismatch alone, ($\lambda \neq 1$ at $\theta = 0^\circ$), produces an array of edge dislocations. Presence of both, an orientation mismatch and a lattice mismatch, produces an array of mixed dislocations[42]. The density of square regions increases with increase in mismatch[42]. Figure 3 shows formation of Moiré patterns[63] between shape complementary pillar samples. Figure 3a(i) represents geometrically the formation of screw dislocations when red and black square lattices overlap at a 5° misorientation. As noted above, the black arrow lines in Fig 3 represent dislocation lines. A corresponding pattern can also be clearly seen on the interface of our actual pillar samples in figure 3a(ii) for the same misorientation angle.

As sliding begins, pillars are pushed into contact, each with a neighboring pillar with force that changes with displacement until it loses contact with its partner pillar. This process occurs for each pillar. In the micrographs of Fig. 3, we observe a pattern of light and dark regions. The lighter patterns correspond to when pillars from complementary surfaces are in partial or full registry (i.e., right next to each other). The darker regions are where pillars from both samples are bent on top of each other and are at maximum disregistry. The lines connecting dark regions can be interpreted to be dislocation lines.

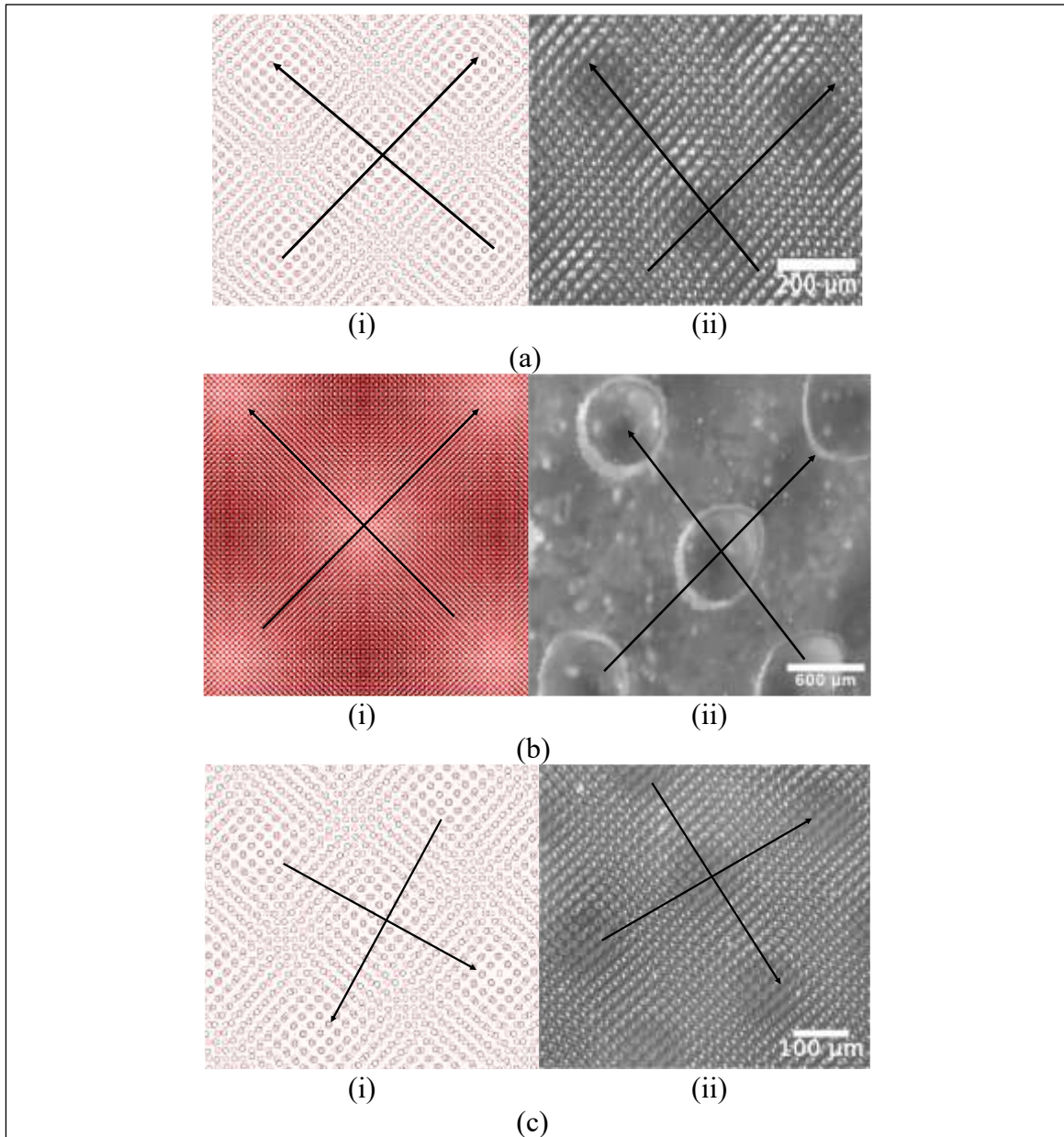


Figure 3. Moiré pattern & Dislocation lines

Representation of Moiré patterns as screw, edge, and mixed dislocations. (3a)(i) An array of screw dislocations produced by aligning red and black lattices at a misorientation, $\theta = 5^\circ$ and $\lambda(a/a')=1$. (3a)(ii) An array of screw dislocations formed at the interface of two pillar samples in contact. (3b)(i) An array of edge dislocations produced when two lattices (here, red and black) have a lattice mismatch, $\lambda(a/a')=1.023$. (3b)(ii) An array of edge dislocations formed at the interface of two pillar samples in contact at $\lambda(a/a')=1.023$. Note difference in scale between 3a(ii) and 3b(ii). (3c) (i) An array of mixed dislocations produced by aligning the two lattices at a misorientation $\theta = 5^\circ$ and at lattice mismatch, $\lambda(a/a')=1.023$. (3c)(ii) An array of mixed dislocations on the pillar interface with the same conditions as 3c(i).

Figure 3b compares the formation of Moiré patterns corresponding to edge dislocations geometrically and in experiments. Figure 3b(i) shows that red and black lattices with $\lambda=1.023$ form edge dislocations. Similar patterns are observed experimentally as shown in Fig 3b(ii). Edge dislocations appear on a perfectly aligned interface with lattice mismatch. As misorientation is then increased from $\theta=0^\circ$, Moiré patterns corresponding to mixed dislocations appear on the interface (shown in 3c). Figure 3b(ii) represents experimentally observed edge dislocations at $\lambda = 1.023 \pm 0.001$. The pattern again shows light and dark regions. Figure 3c(i) represents Moiré patterns corresponding to dislocations with mixed edge and a screw character for $\lambda=1.023$ and $\theta=5^\circ$. The patterns are different than that of screw dislocations if observed carefully in that they are tilted slightly compared to the orientation of screw dislocations. Figure 3c(ii) represents mixed dislocations for pillar samples in contact at $\lambda = 1.023 \pm 0.001$ and $\theta = 5^\circ$. A more detailed account of the geometry of dislocation arrays can be found in [42]. For completeness, we provide the main results. These are that the dislocation density ρ and orientation α of the dislocation lines are functions of misorientation angle, θ , and lattice mismatch, λ . Orientation, α is found as,

$$\alpha = \tan^{-1} \frac{\sin \theta}{\lambda - \cos \theta}, \text{ and} \quad (1)$$

$$\text{density as } \rho = \frac{1}{b} \sqrt{(\lambda - 1)^2 + 4\lambda \sin^2 \left(\frac{\theta}{2}\right)} \quad (2)$$

where b is the magnitude of the Burgers vector, λ is lattice mismatch, and θ is misorientation.

To further analyze the orientation of moving dislocations, it is useful to consider the Peach-Koehler force [58], which is a configurational force that defines the direction of dislocation motion. It is given by

$$F_{PK} = (\sigma \cdot b) \times \xi, \quad (3)$$

where σ is applied stress, b is the Burgers vector and ξ is the dislocation line vector (see fig 4a and 4b for frame of reference). For a screw dislocation as shown in Fig S17d, Burgers vector, b_1 is associated with the dislocation line AA'' and b_2 is associated with dislocation line $C'C''$. Thus,

for a screw dislocation, there are two Burgers vectors i.e., $b_1 = -\frac{1}{\sqrt{2}} \bar{e}_1 + \frac{1}{\sqrt{2}} \bar{e}_2$ and $b_2 = \frac{1}{\sqrt{2}} \bar{e}_1 + \frac{1}{\sqrt{2}} \bar{e}_2$, ξ is the dislocation line vector, $\xi_1 = -\frac{1}{\sqrt{2}} \bar{e}_1 + \frac{1}{\sqrt{2}} \bar{e}_2$, and $\xi_2 = \frac{1}{\sqrt{2}} \bar{e}_1 + \frac{1}{\sqrt{2}} \bar{e}_2$ and stress,

$\sigma = -\tau e_2 \otimes e_3 - \tau e_3 \otimes e_2 + p e_3 \otimes e_3$, thus, $F_{PK} = \tau \left(\frac{1}{2} \bar{e}_1 + \frac{1}{2} \bar{e}_2 \right)$ and $F_{PK} = \tau \left(\frac{1}{2} \bar{e}_1 - \frac{1}{2} \bar{e}_2 \right)$.

This gives the resultant force in \bar{e}_1 direction and this implies that screw dislocation runs perpendicular to the direction of sliding which is true as shown in fig 4b (Full video in

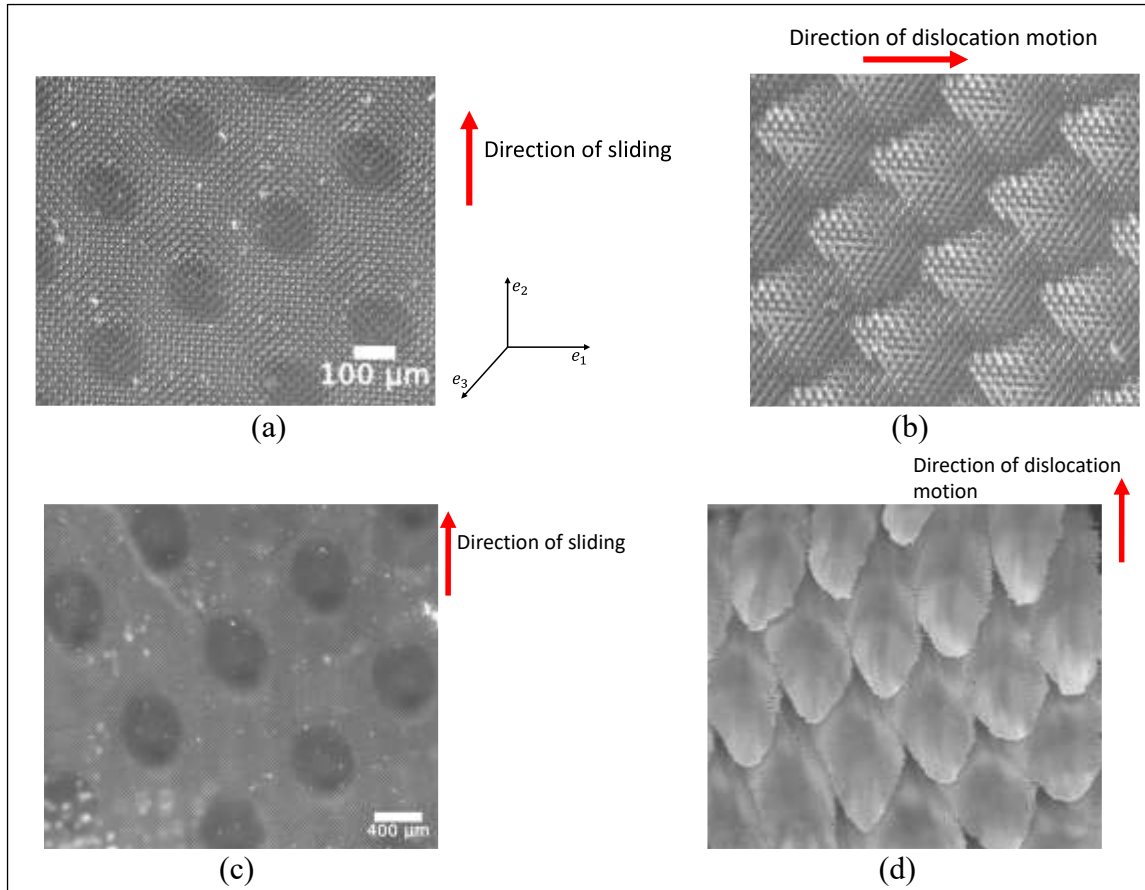


Figure 4. Sliding happens through dislocation glide.

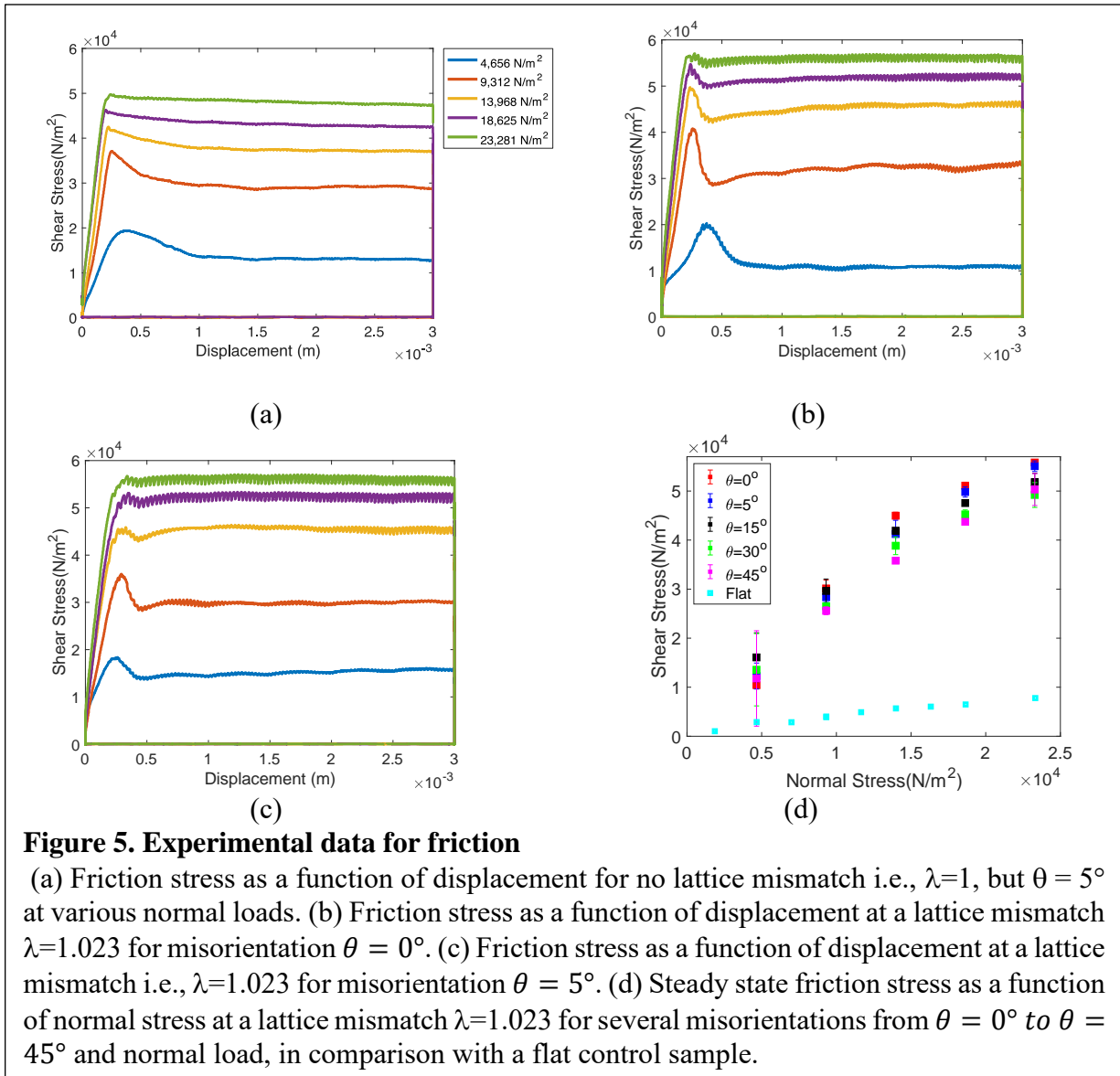
Optical images of pillar interface. (a) Screw dislocations: at misorientation, $\theta = 5^\circ$, $\lambda = 1$ (before sliding commences), (b) Snapshot of sliding screw dislocations at misorientation, $\theta = 5^\circ$, $\lambda = 1$. For sliding in '2' direction, the dislocation pattern moves in '1' direction. (c) Edge dislocations: at misorientation, $\theta = 0^\circ$, $\lambda = 1.023$ (before sliding commences), (d) Snapshot of sliding edge dislocation pattern at $\lambda = 1.023$. For sliding in '2' direction, the dislocation pattern moves in '2' direction.

Supplementary Information, SI: V3_lambda=1_5_deg_ScrewDislocation.avi). For an edge dislocation as shown in Figure S17e, Burgers vector b_1 is associated with dislocation line $C'C''$ and Burgers vector b_2 is associated with dislocation line $A'A''$. Thus, $b_1 = \frac{1}{\sqrt{2}}e_1 - \frac{1}{\sqrt{2}}e_2$, $b_2 = \frac{1}{\sqrt{2}}e_1 + \frac{1}{\sqrt{2}}e_2$, and corresponding dislocation line vector, $\xi_1 = \frac{1}{\sqrt{2}}e_1 + \frac{1}{\sqrt{2}}e_2$, $\xi_2 = -\frac{1}{\sqrt{2}}e_1 + \frac{1}{\sqrt{2}}e_2$, thus, $F_{PK} = \tau \left(-\frac{1}{2} \bar{e}_1 + \frac{1}{2} \bar{e}_2 \right)$ and $F_{PK} = \tau \left(\frac{1}{2} \bar{e}_1 + \frac{1}{2} \bar{e}_2 \right)$ respectively. Net resultant force, F_{PK} is in \bar{e}_2 direction, which implies that for an edge dislocation, dislocation lines run parallel to the direction of sliding as shown in Figs. 4c, d and a full video in Supplementary Information (SI: V8_lambda=1.023_0deg_EdgeDislocation).

Figs. S17 and 4 show that, as we traverse the sample, the registry between pillars above and below the interface varies systematically and periodically, with period identical to that of the Moiré pattern. We see that the direction of dislocation motion is consistent with that given by the Peach-Koehler formula. When sliding initiates, the interface loses its symmetry (compare Figs 4 a,b and c,d). The period of the Moiré pattern corresponds to disregistry equal to the Burgers vector. Therefore, for one Burgers vector of slip in the ‘2’ direction, each pillar undergoes a full load-release cycle. This observation is key for our calculation of macroscopic friction stress. That is, at any point in time, the instantaneous friction force is the sum of all pairwise inter-pillar contact forces across the interface. The friction force averaged over one sliding cycle (slip = Burgers vector) can be obtained by matching external work done to the energy loss for each pillar pair in going through a full loading-unloading cycle.

3.2 Friction Stress Measurements

Figure 5 (a) shows typical raw data for measured friction stress as a function of sliding distance, for different values of normal stress varying from $4 \cdot 10^3 \text{ N/m}^2$ to $2.5 \cdot 10^4 \text{ N/m}^2$ at $\lambda = 1$ and $\theta = 5^\circ$ (dislocations have screw character). As the pillar samples come in contact and start sliding, friction force first rises and then subsides to an approximately constant value. Note that the friction stress increases with increasing normal stress. (Friction stress is obtained by averaging friction force when it stabilizes between 2 to 3 mm of shear displacement and then dividing it by the nominal area of contact, which in this case is sample size i.e., $4 \cdot 4 \text{ mm}^2$.) Fig. 5b shows how the friction stress varies with displacement for edge dislocation case at $\lambda = 1.023$ and $\theta = 0^\circ$. Fig. 5c shows data for friction stress versus displacement for mixed dislocation case at $\lambda = 1.023$ and $\theta =$



5° . The data show that friction stress is strongly dependent on pressure and does not depend much on edge or screw character of dislocation nor on misorientation if λ is close to unity.

Figure 5d shows a plot of how friction stress varies as a function of normal load and misorientation, θ . This particular case is at $\lambda=1.023$ for various values of $\theta = 0^\circ, 5^\circ, 15^\circ, 30^\circ$ and 45° . As can be seen from the figure 5d, friction rises strongly with the normal stress but is essentially independent of misorientation. This is starkly different from that found in the ridge-channel geometry [43] where friction depends strongly on misorientation angle. Weak dependence on misorientation for pillar samples is likely because pillars are organized in a square lattice, which is not far from isotropic. Also shown in Fig. 5(d) is measured friction stress for a control in which one of the pillar

interfaces is replaced by a flat, unstructured, PDMS sample. Friction for cases where both sides have pillars shows significant increase as compared to friction in the control case. Friction stress for pillar complementary samples can be seen to be enhanced by up to about a factor of 5 over that of a control sample.

We turn our attention next to studying the relationship between macroscopically observed friction and the pairwise interaction of pillars. For this purpose, we first show results on single pillar-pair experiments and then combine these with a geometric model of the sliding interface to calculate predicted macroscopic friction stress.

3.3 Single pillar-pair friction experiments

We propose that the friction force arises from the ensemble of pillar-pillar interactions. To study this quantitatively and directly, we first conduct experiments on the interaction of pairs of pillars. Single pillar samples are fabricated following the process mentioned in section 2.1. Pairs of these single-pillar samples are slid past each other. The contact is characterized by two types of overlaps between pillars: in the plane of the interface (lateral overlap) and along the length of the undeformed pillar (vertical overlap or H_c as height of contact) as shown in Figs. 2d, e; 6a, b.

The experiments are performed keeping the vertical distance between two pillars fixed. Let the vertical distance be d and length of each pillar, L . If the gap exceeds the upper limit ($d > L$), we have zero vertical overlap. Then the pillars disengage and the force they transmit to each other while sliding goes to zero. If the gap hits the lower limit ($d = L$), then the pillar can take any vertical load.

Fig 6a represents a lateral overlap that varies from 0 to 1, where l_x is a dimensionless parameter to measure lateral overlap and is defined as, $l_x = 1 - \frac{\Delta x}{2R}$. Fig 6b represents vertical overlap along

the length of the pillar and is defined as $l_z = \frac{H_c}{L}$. Figure 6c-h shows a schematic progression of sliding a pair of pillars past each other. The collection of forces resisting this motion give rise to

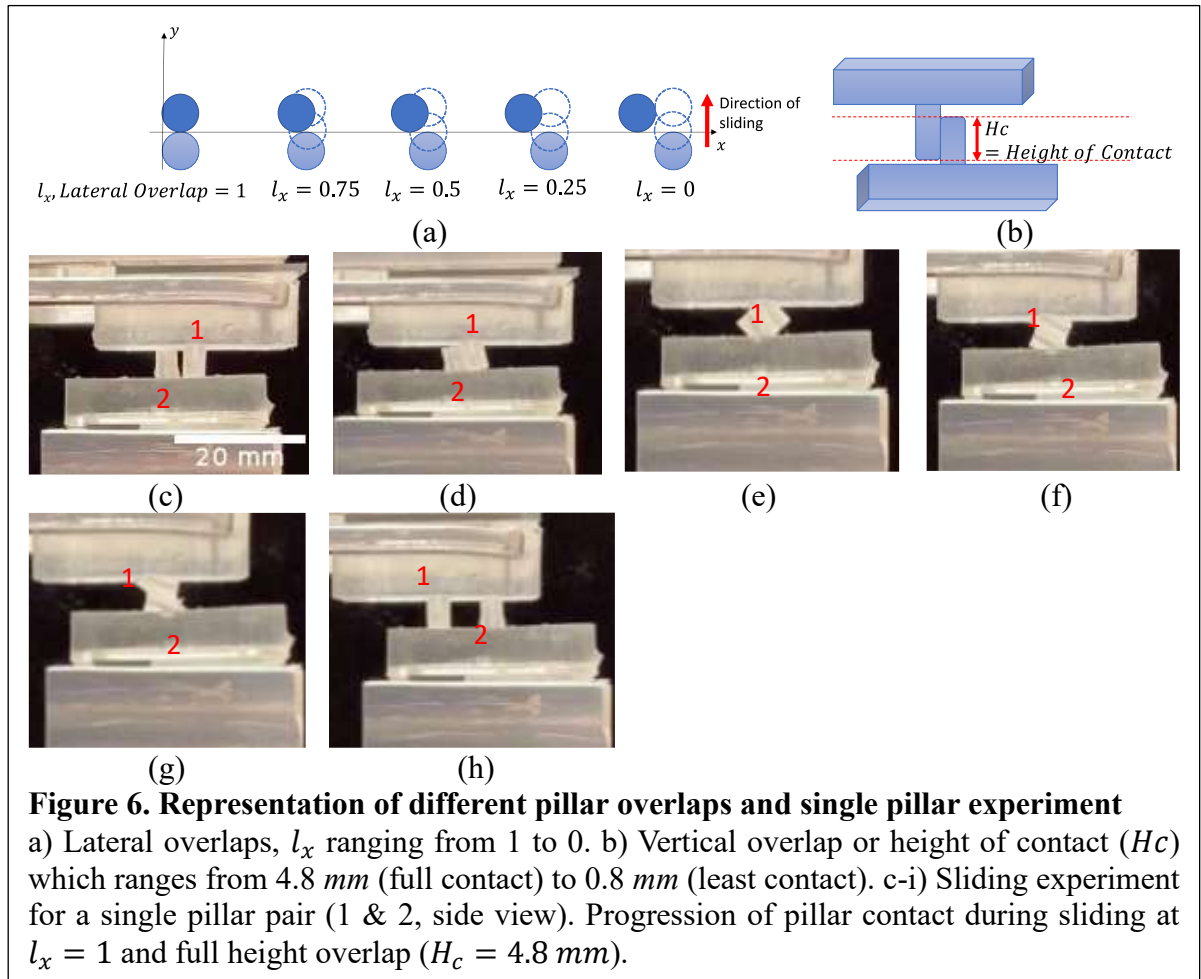


Figure 6. Representation of different pillar overlaps and single pillar experiment

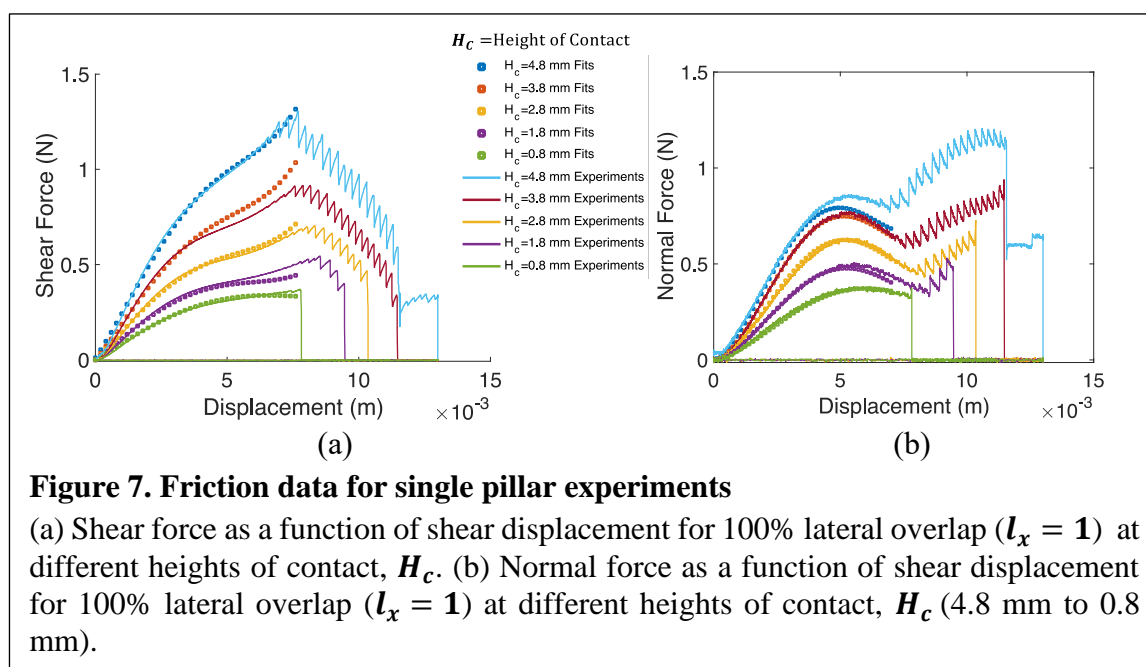
a) Lateral overlaps, l_x ranging from 1 to 0. b) Vertical overlap or height of contact (H_c) which ranges from 4.8 mm (full contact) to 0.8 mm (least contact). c-i) Sliding experiment for a single pillar pair (1 & 2, side view). Progression of pillar contact during sliding at $l_x = 1$ and full height overlap ($H_c = 4.8$ mm).

the macroscopic friction force as well as the vertical reaction force.

Neglecting the role of adhesion (see experiments in SI section S3 on lubricated vs. dry single pillar pair experiments), we make the approximation that if we normalize all displacements and location by pillar radius and stresses by the shear modulus, then the normalized stress is a function of normalized location. That is, if one scales the system uniformly, forces measured in the pillar-pair interaction experiments can simply be scaled down to estimate forces in the micropillar samples. A series of figures in Figs.6c-h shows progression of sliding for a typical single pillar-pair experiment. The corresponding shear and normal force plots are shown in Figure 7 as a function of shear displacement. As the sliding starts under normal displacement control (i.e., vertical overlap is fixed for each experiment and normal load varies), the two

pillars come in contact and bend as shear displacement increases. The two pillars appear to stick to each other as shear stress/force reaches a maximum point and then series of slipping events occur, accompanied by decrease of shear force, and ending with separation of the two pillars. (The case shown here in Fig.7 c-h is for a 100% lateral overlap ($l_x = 1$)).

Figure 7a shows variation of shear force with sliding displacement for single pillar pair experiments for lateral overlap, $l_x = 1$ at different vertical overlaps ranging from (4.8 mm to 0.8 mm). Shear force is maximum for maximum lateral overlap ($l_x = 1$) and $H_c = 4.8$ mm and decreases if the lateral overlap or height of contact is decreased (as shown in section S3 in SI). After contact, the shear force initially increases linearly with shear displacement. At



an intermediate shear displacement, the response softens and then hardens again prior to initiation of stick-slip. As seen from Fig 7a, after shear displacement reaches ~ 8 mm, there is a decline in shear force as the pillars slide with respect to each other in stick-slip steps. This stick slip motion as the force declines is most significant in the 100% lateral overlap case whereas the force drop in the rest of the cases ($l_x = 0.75, 0.5, 0.25, 0$) is more sudden (shown in SI). Normal force, on the other hand, rises initially but declines as shear force slope increases. This is because the two pillars in contact are almost horizontal (more force in shear direction) and thus normal force declines.

Figure 7 a, b also shows quartic fits to the experimental data. The detailed mechanics of this inter-pillar interaction is presented in a companion paper.

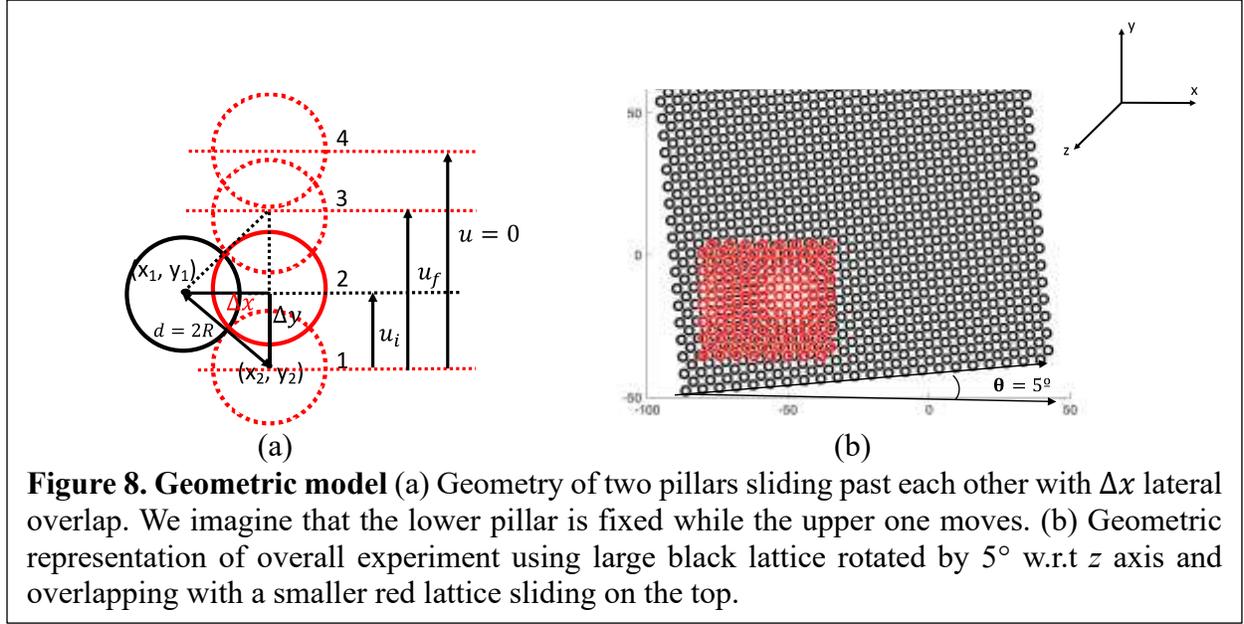
The single-pair pillar experiments provide:

$$\begin{aligned} & T(u_s), N(u_s), u^* \\ & w = \int_0^{u^*} T(u_s) du_s \end{aligned} \tag{4}$$

where, T , N , u^* , u_s , and w are shear force, normal force, maximum shear displacement, shear displacement, and energy loss from a single pillar pair, respectively. As shown in SI, the effect of adhesion is negligible so that change of scale leaves all stresses unchanged. Therefore, if the scale factor between the single pillar-pair experiments and the pillar array is α_s , then energy scales as $(\alpha_s)^3$, displacement by α_s , and forces by $(\alpha_s)^2$. Thus, for given overlap between a pair of micropillars, we may use the results of the mm-scale single pillar pair experiments to compute the shear and normal force of interaction for given lateral and vertical overlap of a pair of micro-pillars.

Each single-pillar-pair experiment is conducted for five specified values of lateral and vertical overlap ($5 \times 5 = 25$ cases in all) producing data such as shown in Fig. 7 a, and b (see also SI, Figs S7-8). Each force plot is fit with four fitting parameters. Each fitting parameter is a function of the two overlap parameters i.e., lateral overlap and vertical overlap or height of contact (H_C). Thus, we have a 2D surface for each parameter (more information provided in SI Figure S15) that is fit by a third order polynomial in two variables (lateral and vertical overlaps) using which we can estimate the shear and normal forces for any specified overlaps.

3.4 Overall friction response



This section presents a geometric model illustrating the interaction between cylindrical pillars as they slide past one another. Fig. 8(a) shows two circles (representing pillars) sliding past each other with some lateral overlap, $l_x = \frac{\Delta x}{2R}$. Here, Δx denotes the lateral displacement between the centers of the two pillars, and R is the radius of each pillar. The upper pillar is shown in a sequence of positions (numbered 1 to 4) as it moves vertically by a distance ‘ dy ’ at each step. The deflection, δ , which quantifies the deviation of the pillars from their initial positions during sliding, is determined for each step. The deflection is expressed as:

$$\delta = \begin{cases} 2R - d & , & 2R - d > 0 \\ 0 & , & 2R - d < 0 \end{cases} \quad (5)$$

where d represents the distance between the centers of the two pillars and is calculated using the equation:

$$d = \sqrt{\Delta x^2 + \Delta y^2}; \Delta x = x_2 - x_1; \Delta y = y_2 - y_1 \quad (6)$$

thus, deflection simplifies to $\delta = 2R - \sqrt{\Delta x^2 + \Delta y^2}$, when $2R > d$.

The final displacement in sliding direction, u_f , is derived from the initial displacement at which the pillars first come into contact, denoted as u_i , and is defined by:

$$u_f(\text{Final displacement}) = -(\Delta y - u_i) \quad (0 \leq u_f \leq 4R) \quad (7)$$

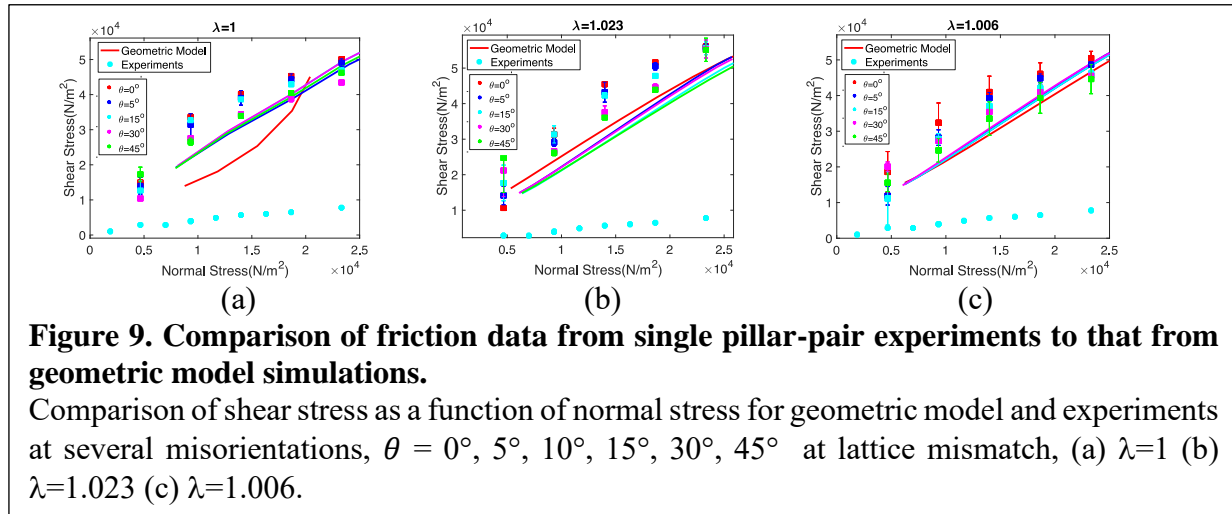
This calculation also mirrors the physical bending of single pillars observed in sliding experiments. As the red lattice slides over the black lattice, the model calculates the displacement (in sliding direction) of each red pillar at every point in time, setting the displacement to zero once the distance between the centers of the pillars exceeds $2R$. Initial displacement is defined as,

$$u_i = \sqrt{((2 * R)^2 - \Delta x^2)}, \quad (8)$$

which indicates the displacement at which pillars begin to overlap.

Fig. 8(b) visualizes the overall experimental setup with stationary lattice of large black pillars rotated by 5° with respect to z-axis, and a lattice of smaller red pillars sliding over the black lattice. The aim is to calculate shear stress that arises due to interaction between overlapping pillars. In the sliding lattice model, the calculation of shear and normal force begins with the determination of the final displacement, u_f of each red pillar, which is analogous to the physical displacement observed in single pillar sliding experiments (Fig. 7a & 7b). This final displacement is tracked until the inter-pillar distance exceeds twice the radius, effectively reducing the displacement to zero for calculation purposes.

The force-versus-displacement curves derived from single pillar experiments are processed through a quartic polynomial fitting procedure (with zero intercept). This yielded a set of four coefficients for each curve, and these coefficients are functions of two parameters: the lateral overlap, l_x and the height of contact, H_c . Through this functional relationship, we formulated a series of surface functions that map the dependency of these coefficients on the overlap parameters.



The simulation is carried out for fixed gap and this functional mapping allows us to interpolate between measured overlaps for predicting the system's response to varying degrees of overlap between the pillars. To provide a visual illustration of these relationships, contour plots for each surface function have been included in Figure S15a and S15b.

With the surface functions defined, we are able to determine the coefficients for any specified combination of lateral and height overlaps. These coefficients, when applied in conjunction with the final displacement values, enable us to compute the shear and normal force. This approach allows for an accurate quantification of shear and normal forces. These individual forces from pairs of pillars are subsequently summed and divided by the sample area to ascertain the average shear and normal stress across the lattice.

The shear stress vs normal stress predictions yielded by our model align closely with the empirical data from microscale friction experiments, remaining within the experimental shear stress range. Figures 9(a), 9(b) and 9(c) display the comparison of shear stress versus normal stress values obtained from the model with experimental data for various values of λ and θ .

Figure 9a presents a comparative analysis of shear stress versus normal stress, specifically for a lattice parameter, λ , set to 1 across various angles of rotation, θ . The correlation between the model's predictions and the experimental data is generally favorable, however, an anomaly is observed for the case where $\theta = 0^\circ$, the red curve. In this specific instance, the model predicts a sawtooth pattern in the shear force curve, diverging from the experimental trend. This deviation is attributed to the absence of edge-nucleated dislocations within the model's framework for the $\theta = 0^\circ$ scenario. Consequently, the sawtooth pattern leads to a lower average shear stress in comparison to both the experimental data and the other curves represented for different θ values.

For a more detailed theoretical underpinning, including a comparison with a one-dimensional edge dislocation model, readers are directed to the Supplementary Information section S4. This section discusses how the force summation approach used here aligns with energetic methods traditionally employed in the computation of average friction stress. See also section S6 in SI, which contains a simple model that shows why summation of forces calculated using isolated pairs of pillars works because the pillars are highly compliant.

4. Summary and Conclusions

We presented a study of friction of shape-complementary pillar interfaces. The structure of the interface can be understood to comprise Moiré patterns that accommodate misorientation and differences in lattice spacing on two sides of the interface. Relative sliding of such complementary pillar structures can be viewed as being accommodated by glide of Moiré patterns. The frictional force depends strongly on pressure but only weakly on misorientation. Friction for complementary pillar structures is higher than that of control samples by up to a factor of 5. In order to relate macroscopic measured friction to the behavior of single pillar-pair interactions, we conducted mm-scale single pillar-pair experiments and obtained pillar-pillar interaction forces at the interface. Using these data, we developed a simple numerical model to determine the sliding friction of the pillar interface as a sum of pairwise pillar-pillar interactions. Our model compares well with experiments.

This pillar interface has many similarities to atomistic interfaces. The interaction of atoms inside the dislocation core determines the force required to move a dislocation. In our case, the relevant interaction is that between pillars on opposite sides of the interface. An important difference between our interfacial structure and that found in crystalline interfaces at the atomic scale is that the summed mechanics of pillar pairs suffices to obtain the total friction stress. That is, pillar-pillar coupling is very stiff. In SI S6 we present a simple model for an incommensurate pillar pair array which shows how, for sufficiently stiff pillars the system would behave more like atomistic interfaces do, with disregistry confined to dislocation lines.

Our results show how shape complementary pillar interfaces can be designed for enhanced, sliding friction.

5. Statements

The authors declare no conflict of interest.

6. Acknowledgements

We acknowledge support from the National Science Foundation through the Grant LEAP-HI: CMMI-1854572. We would also like to acknowledge useful discussion with Mike Andrews.

- 7. Data Availability:** The data presented in this paper are available from the authors on reasonable request.

8. References

- [1] C. Menon, M. Murphy, and M. Sitti, "Gecko inspired surface climbing robots," in *2004 IEEE international conference on robotics and biomimetics*, 2004: IEEE, pp. 431-436.
- [2] M. Zhou, Y. Tian, D. Sameoto, X. Zhang, Y. Meng, and S. Wen, "Controllable interfacial adhesion applied to transfer light and fragile objects by using gecko inspired mushroom-shaped pillar surface," *ACS applied materials & interfaces*, vol. 5, no. 20, pp. 10137-10144, 2013.
- [3] T. Eisner and D. J. Aneshansley, "Defense by foot adhesion in a beetle (*Hemisphaerota cyanea*)," (in eng), *Proc Natl Acad Sci U S A*, vol. 97, no. 12, pp. 6568-73, Jun 6 2000, doi: 10.1073/pnas.97.12.6568.
- [4] K. Autumn, "Gecko Adhesion: Structure, Function, and Applications," *MRS Bulletin*, vol. 32, no. 6, pp. 473-478, 2007/06/01 2007, doi: 10.1557/mrs2007.80.
- [5] C. Creton and S. N. Gorb, "Sticky feet: from animals to materials," *Mrs Bulletin*, vol. 32, pp. 466-468, 2007.
- [6] A. Jagota and C.-Y. Hui, "Adhesion, friction, and compliance of bio-mimetic and bio-inspired structured interfaces," *Materials Science and Engineering: R: Reports*, 2011, doi: 10.1016/j.mser.2011.08.001.
- [7] K. Autumn *et al.*, "Adhesive force of a single gecko foot-hair," *Nature*, vol. 405, no. 6787, pp. 681-685, 2000.
- [8] K. Autumn and A. M. Peattie, "Mechanisms of adhesion in geckos," *Integrative and comparative biology*, vol. 42, no. 6, pp. 1081-1090, 2002.
- [9] B. Bhushan, "Bioinspired structured surfaces," *Langmuir*, vol. 28, no. 3, pp. 1698-714, Jan 24 2012, doi: 10.1021/la2043729.
- [10] B. Bhushan, "Adhesion of multi-level hierarchical attachment systems in gecko feet," *Journal of Adhesion Science and Technology*, vol. 21, no. 12-13, pp. 1213-1258, 2007, doi: 10.1163/156856107782328353.
- [11] M. S. Kellar Autumn, Yiching A. Liang, Anne M. Peattie, Wendy R. Hansen, Simon Sponberg, Thomas W. Kenny, Ronald Fearing, Jacob N. Israelachvili, and Robert J. Full, "Evidence for van der Waals adhesion in gecko setae," 2002.
- [12] H. Lee, B. P. Lee, and P. B. Messersmith, "A reversible wet/dry adhesive inspired by mussels and geckos," *Nature*, vol. 448, no. 7151, pp. 338-41, Jul 19 2007, doi: 10.1038/nature05968.
- [13] S. N. Gorb, "Evolution of the Dragonfly Head-Arresting System," *Proceedings: Biological Sciences*, vol. 266, no. 1418, pp. 525-535, 1999. [Online]. Available: <http://www.jstor.org/stable/51177>.
- [14] R. G. Beutel and S. N. Gorb, "Ultrastructure of attachment specializations of hexapods (Arthropoda): evolutionary patterns inferred from a revised ordinal phylogeny," *Journal of Zoological Systematics and Evolutionary Research*, vol. 39, no. 4, pp. 177-207, 2001, doi: 10.1046/j.1439-0469.2001.00155.x.
- [15] W. Federle, E. L. Brainerd, T. A. McMahon, and B. Hölldobler, "Biomechanics of the movable pretarsal adhesive organ in ants and bees," *Proceedings of the National Academy of Sciences*, vol. 98, no. 11, pp. 6215-6220, 2001, doi: doi:10.1073/pnas.111139298.
- [16] J. A. Peterson, "Convergent and Alternative Designs in the Digital Adhesive Pads of Scincid Lizards," 1982.

- [17] H. A. Stone, "Biological Micro- and Nanotribology: Nature's Solutions," *Physics Today*, vol. 55, no. 6, pp. 53-53, 2002, doi: 10.1063/1.1496378.
- [18] A. Kesel, A. Martin, and T. Seidl, "Adhesion measurements on the attachment devices of the jumping spider *Evarcha arcuata*," *Journal of Experimental Biology*, vol. 206, no. 16, pp. 2733-2738, 2003.
- [19] Z. Dai, S. N. Gorb, and U. Schwarz, "Roughness-dependent friction force of the tarsal claw system in the beetle *Pachnoda marginata* (Coleoptera, Scarabaeidae)," *Journal of experimental biology*, vol. 205, no. 16, pp. 2479-2488, 2002.
- [20] C. G. Ara'nzazu del Campo, and Eduard Arzt, "contact shape controls adhesion of bioinspired fibrillar structures," 2007.
- [21] S. N. Gorb, "Biological attachment devices: exploring nature's diversity for biomimetics," *Philosophical Transactions of the Royal Society A: Mathematical, Physical and Engineering Sciences*, vol. 366, no. 1870, pp. 1557-1574, 2008.
- [22] D. R. King, M. D. Bartlett, C. A. Gilman, D. J. Irschick, and A. J. Crosby, "Creating gecko-like adhesives for "real world" surfaces," *Advanced Materials*, vol. 26, no. 25, pp. 4345-4351, 2014.
- [23] S. N. Gorb *et al.*, "Structural design and biomechanics of friction-based releasable attachment devices in insects," *Integrative and Comparative Biology*, vol. 42, no. 6, pp. 1127-1139, 2002.
- [24] M. Piccardo, A. Chateauminois, C. Fretigny, N. M. Pugno, and M. Sitti, "Contact compliance effects in the frictional response of bioinspired fibrillar adhesives," *Journal of The Royal Society Interface*, vol. 10, no. 83, p. 20130182, 2013.
- [25] M. Scherge and S. Gorb, *Biological micro-and nanotribology*. Springer Science & Business Media, 2001.
- [26] M. D. Bartlett, A. B. Croll, D. R. King, B. M. Paret, D. J. Irschick, and A. J. Crosby, "Looking beyond fibrillar features to scale gecko-like adhesion," *Advanced Materials*, vol. 24, no. 8, pp. 1078-1083, 2012.
- [27] H. Gao, X. Wang, H. Yao, S. Gorb, and E. Arzt, "Mechanics of hierarchical adhesion structures of geckos," *Mechanics of materials*, vol. 37, no. 2-3, pp. 275-285, 2005.
- [28] E. Arzt, S. Gorb, and R. Spolenak, "From micro to nano contacts in biological attachment devices," *Proceedings of the National Academy of Sciences*, vol. 100, no. 19, pp. 10603-10606, September 16, 2003 2003, doi: 10.1073/pnas.1534701100.
- [29] M. G. De, "Velvet type fabric and method of producing same," ed: Google Patents, 1955.
- [30] S. Gorb, "ATTACHMENT DEVICES OF INSECT CUTICLE," 2001.
- [31] N. J. Glassmaker, A. Jagota, C.-Y. Hui, W. L. Noderer, and M. K. Chaudhury, "Biologically inspired crack trapping for enhanced adhesion," *Proceedings of the National Academy of Sciences*, vol. 104, no. 26, pp. 10786-10791, 2007.
- [32] M. Kamperman, E. Kroner, A. del Campo, R. M. McMeeking, and E. Arzt, "Functional adhesive surfaces with "gecko" effect: The concept of contact splitting," *Advanced Engineering Materials*, vol. 12, no. 5, pp. 335-348, 2010.
- [33] N. J. Glassmaker, T. Himeno, C. Y. Hui, and J. Kim, "Design of biomimetic fibrillar interfaces: 1. Making contact," *J R Soc Interface*, vol. 1, no. 1, pp. 23-33, Nov 22 2004, doi: 10.1098/rsif.2004.0004.
- [34] B. Wijerathne, T. Liao, K. Ostrikov, and Z. Sun, "Bioinspired Robust Mechanical Properties for Advanced Materials," *Small Structures*, vol. 3, no. 9, 2022, doi: 10.1002/ssstr.202100228.

- [35] R. Hensel, K. Moh, and E. Arzt, "Engineering micropatterned dry adhesives: from contact theory to handling applications," *Advanced Functional Materials*, vol. 28, no. 28, p. 1800865, 2018.
- [36] B. Bhushan, "Biomimetics," *Philos Trans A Math Phys Eng Sci*, vol. 367, no. 1893, pp. 1443-4, Apr 28 2009, doi: 10.1098/rsta.2009.0026.
- [37] M. R. WALTER FEDERLE, ADAM S.G. CURTIS, AND ROBERT J. FULL, "An Integrative Study of Insect Adhesion: Mechanics and Wet Adhesion of Pretarsal Pads in Ants'," 2002.
- [38] S. Kim and M. Sitti, "Biologically inspired polymer microfibers with spatulate tips as repeatable fibrillar adhesives," *Applied physics letters*, vol. 89, no. 26, p. 261911, 2006.
- [39] J. Purto, M. Frensemeier, and E. Kroner, "Switchable adhesion in vacuum using bio-inspired dry adhesives," *ACS applied materials & interfaces*, vol. 7, no. 43, pp. 24127-24135, 2015.
- [40] C. M. Chen, C. L. Chiang, C. L. Lai, T. Xie, and S. Yang, "Buckling-Based Strong Dry Adhesives Via Interlocking," (in English), *Advanced Functional Materials*, vol. 23, no. 30, pp. 3813-3823, Aug 12 2013, doi: 10.1002/adfm.201300052.
- [41] Z. He, Z. Liu, M. Li, C. Y. Hui, and A. Jagota, "Meso-scale dislocations and friction of shape-complementary soft interfaces," *J R Soc Interface*, vol. 18, no. 175, p. 20200940, Feb 2021, doi: 10.1098/rsif.2020.0940.
- [42] J. Dillen, Z. He, C.-Y. Hui, and A. Jagota, "Geometry of defects at shape-complementary soft interfaces," *Extreme Mechanics Letters*, vol. 9, pp. 74-83, 2016.
- [43] A. K. Singh, Y. Bai, N. Nadermann, A. Jagota, and C. Y. Hui, "Adhesion of microchannel-based complementary surfaces," *Langmuir*, vol. 28, no. 9, pp. 4213-22, Mar 6 2012, doi: 10.1021/la204519w.
- [44] C. Jin, A. Jagota, and C.-Y. Hui, "Structure and Energetics of Dislocations at Micro-Structured Complementary Interfaces Govern Adhesion," *Advanced Functional Materials*, vol. 23, no. 27, pp. 3453-3462, 2013, doi: 10.1002/adfm.201203337.
- [45] S. Vajpayee, K. Khare, S. Yang, C.-Y. Hui, and A. Jagota, "Adhesion Selectivity Using Rippled Surfaces," *Advanced Functional Materials*, vol. 21, no. 3, pp. 547-555, 2011, doi: 10.1002/adfm.201001652.
- [46] P. Guduru, "Detachment of a rigid solid from an elastic wavy surface: theory," *Journal of the Mechanics and Physics of Solids*, vol. 55, no. 3, pp. 445-472, 2007.
- [47] P. Guduru and C. Bull, "Detachment of a rigid solid from an elastic wavy surface: Experiments," *Journal of the Mechanics and Physics of Solids*, vol. 55, no. 3, pp. 473-488, 2007.
- [48] Y. Desplanques, "Amontons-Coulomb Friction Laws, A Review of the Original Manuscript," *SAE International Journal of Materials and Manufacturing*, vol. 8, no. 1, pp. 98-103, 2014, doi: 10.4271/2014-01-2489.
- [49] M. Urbakh and E. Meyer, "Nanotribology: The renaissance of friction," *Nat Mater*, vol. 9, no. 1, pp. 8-10, Jan 2010, doi: 10.1038/nmat2599.
- [50] A. Vanossi, N. Manini, M. Urbakh, S. Zapperi, and E. Tosatti, "Colloquium: Modeling friction: From nanoscale to mesoscale," *Reviews of Modern Physics*, vol. 85, no. 2, pp. 529-552, 2013, doi: 10.1103/RevModPhys.85.529.
- [51] R. Peierls, "The size of a dislocation," *Proceedings of the Physical Society*, vol. 52, no. 1, p. 34, 1940.

- [52] F. Nabarro, "Fifty-year study of the Peierls-Nabarro stress," *Materials Science and Engineering: A*, vol. 234, pp. 67-76, 1997.
- [53] L. Prandtl, "Ein Gedankenmodell zur kinetischen Theorie der festen Körper," *ZAMM - Zeitschrift für Angewandte Mathematik und Mechanik*, vol. 8, no. 2, pp. 85-106, 1928, doi: 10.1002/zamm.19280080202.
- [54] J. R. a. M. O. Robbins, "Understanding and illustrating the atomic origins of friction," 2004.
- [55] A. Ghatak, K. Vorvolakos, H. Q. She, D. L. Malotky, and M. K. Chaudhury, "Interfacial rate processes in adhesion and friction," *Journal of Physical Chemistry B*, vol. 104, no. 17, pp. 4018-4030, 2000.
- [56] S. Sills, K. Vorvolakos, M. K. Chaudhury, and R. M. Overney, "Molecular origins of elastomeric friction," in *Fundamentals of friction and wear*: Springer, 2007, pp. 659-676.
- [57] A. Schallamach, "A theory of dynamic rubber friction," *Wear*, vol. 6, no. 5, pp. 375-382, 1963/09/01/ 1963, doi: [https://doi.org/10.1016/0043-1648\(63\)90206-0](https://doi.org/10.1016/0043-1648(63)90206-0).
- [58] P. M. Anderson, J. P. Hirth, and J. Lothe, *Theory of dislocations*. Cambridge University Press, 2017.
- [59] T. A. Sharp, L. Pastewka, and M. O. Robbins, "Elasticity limits structural superlubricity in large contacts," *Physical Review B*, vol. 93, no. 12, 2016, doi: 10.1103/PhysRevB.93.121402.
- [60] T. A. Sharp, L. Pastewka, V. L. Lignères, and M. O. Robbins, "Scale- and load-dependent friction in commensurate sphere-on-flat contacts," *Physical Review B*, vol. 96, no. 15, 2017, doi: 10.1103/PhysRevB.96.155436.
- [61] W. Bollmann, *Crystal Defects and Crystalline Interfaces*. New York: Springer-Verlag, 1970.
- [62] A. Merkle and L. Marks, "A predictive analytical friction model from basic theories of interfaces, contacts and dislocations," *Tribology Letters*, vol. 26, pp. 73-84, 2007.
- [63] G. O. a. Y. Nishijima, "MOIRÉ PATTERNS," *Scientific American*, vol. 208, No.5, 1963.